










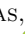







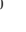




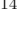
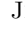







A Highly Eccentric Warm Jupiter Orbiting TIC 237913194

MARTIN SCHLECKER ¹, DIANA KOSSAKOWSKI ¹, RAFAEL BRAHM ^{2,3}, NÉSTOR ESPINOZA ⁴, THOMAS HENNING ¹,
LUDMILA CARONE ¹, KARAN MOLAVERDIKHANI ^{5,1}, TRIFON TRIFONOV ¹, PAUL MOLLIERE ¹,
MELISSA J. HOBSON ³, ANDRÉS JORDÁN ^{2,3}, FELIPE I. ROJAS ^{6,3}, HUBERT KLAHR ¹, PAULA SARKIS ¹,
GÁSPÁR Á. BAKOS ⁷, WAQAS BHATTI ⁷, DAVID OSIP ⁸, VINCENT SUC ^{2,9}, GEORGE RICKER ¹⁰, ROLAND VANDERSPEK ¹⁰,
DAVID W. LATHAM ¹¹, SARA SEAGER ^{10,12,13}, JOSHUA N. WINN ⁷, JON M. JENKINS ¹⁴, MICHAEL VEZIE ¹⁰,
JESUS NOEL VILLASEÑOR ¹⁰, MARK E. ROSE ¹⁴, DAVID R. RODRIGUEZ ⁴, JOSEPH E. RODRIGUEZ ¹¹,
SAMUEL N. QUINN ¹¹ AND AVI SHPORER ¹⁰

¹Max-Planck-Institut für Astronomie, Königstuhl 17, Heidelberg 69117, Germany

²Facultad de Ingeniería y Ciencias, Universidad Adolfo Ibáñez, Av. Diagonal las Torres 2640, Peñalolén, Santiago, Chile

³Millennium Institute for Astrophysics, Chile

⁴Space Telescope Science Institute, 3700 San Martin Drive, Baltimore, MD 21218, USA

⁵Landessternwarte, Zentrum für Astronomie der Universität Heidelberg, Königstuhl 12, 69117 Heidelberg, Germany

⁶Instituto de Astrofísica, Pontificia Universidad Católica de Chile, Av. Vicuña Mackenna 4860, Macul, Santiago, Chile

⁷Department of Astrophysical Sciences, Princeton University, NJ 08544, USA

⁸Las Campanas Observatory, Carnegie Institution of Washington, Colina el Pino, Casilla 601 La Serena, Chile

⁹El Sauce Observatory, Chile

¹⁰Department of Physics and Kavli Institute for Astrophysics and Space Research, Massachusetts Institute of Technology, Cambridge, MA 02139, USA

¹¹Center for Astrophysics | Harvard & Smithsonian, 60 Garden St, Cambridge, MA 02138, USA

¹²Department of Earth, Atmospheric and Planetary Sciences, Massachusetts Institute of Technology, Cambridge, MA 02139, USA

¹³Department of Aeronautics and Astronautics, MIT, 77 Massachusetts Avenue, Cambridge, MA 02139, USA

¹⁴NASA Ames Research Center, Moffett Field, CA 94035, USA

(Received June 1, 2019; Revised January 10, 2020; Accepted October 3, 2020)

ABSTRACT

The orbital parameters of warm Jupiters serve as a record of their formation history, providing constraints on formation scenarios for giant planets on close and intermediate orbits. Here, we report the discovery of TIC 237913194b, detected in full frame images from Sectors 1 and 2 of *TESS*, ground-based photometry (*CHAT*, *LCOGT*), and *FEROS* radial velocity time series. We constrain its mass to $M_P = 1.942^{+0.091}_{-0.091} M_J$ and its radius to $R_P = 1.117^{+0.054}_{-0.047} R_J$, implying a bulk density similar to Neptune's. It orbits a G-type star ($M_\star = 1.026^{+0.057}_{-0.055} M_\odot$, $V = 12.1$ mag) with a period of 15.17 d on one of the most eccentric orbits of all known warm giants ($e \approx 0.58$). This extreme dynamical state points to a past interaction with an additional, undetected massive companion. A tidal evolution analysis showed a large tidal dissipation timescale, suggesting that the planet is not a progenitor for a hot Jupiter caught during its high-eccentricity migration. TIC 237913194b further represents an attractive opportunity to study the energy deposition and redistribution in the atmosphere of a warm Jupiter with high eccentricity.

Keywords: planets and satellites: detection — planets and satellites: fundamental parameters — planets and satellites: gaseous planets — planets and satellites: individual (TIC 237913194b, TOI 2179b) — techniques: photometric — techniques: radial velocities

1. INTRODUCTION

Gravitational interactions among massive planets during their formation and evolution leave an imprint on their orbital parameters. However, these imprints are

frequently erased in the case of hot Jupiters, which are prone to orbital changes through tidal interactions with their host star (e.g., Eggleton et al. 1998). Planets on more distant orbits ($P \gtrsim 10$ d), although not as readily detected, are expected to retain this information and thereby provide valuable insights into the formation history of their planetary system. Unfortunately, the sample of confirmed, nearby transiting warm Jupiters is still small. The transit survey currently performed by the Transiting Exoplanet Survey Satellite (*TESS*, Ricker et al. 2014) is changing that: hundreds of giant planets on intermediate orbits are expected to be detected during the all-sky survey (Sullivan et al. 2015; Barclay et al. 2018). With this in mind, the Warm gIaNts with tEss (WINE, Brahm et al. 2019; Jordán et al. 2020) collaboration embarked on a search for such warm Jupiters. Using a network of photometric and spectroscopic facilities, we identify and follow up *TESS* planet candidates to confirm them, characterize their orbital parameters, and use them to inform planet formation theory.

Here, we report the discovery of a temperate giant planet in a highly eccentric orbit around a G3 star. By the aid of additional ground-based photometry from the *CHAT* and *LCOGT* telescopes, as well as precise radial velocity measurements from *FEROS*, we were able to tightly constrain the planet’s mass, radius, and orbital parameters. It is only the third *TESS* giant planet with $e > 0.3$ (Jordán et al. 2020; Rodríguez et al. 2019), and it has one of the most eccentric orbits reported to date for a warm Jupiter.

We show that its dynamical state is not consistent with a high-eccentricity migration scenario that would eventually result in the planet becoming a hot Jupiter. Instead, a past interaction with an undetected massive body has likely caused the planet’s extreme orbit. This valuable addition to the small sample of known warm Jupiter-hosting systems can help constrain the enigma of their origin. Through its eccentric orbit and the subsequent varying radiative forcing, the planet further holds the promise of observing potential disequilibrium processes in its atmosphere.

This paper is organized as follows: In Section 2 we present the observational data used in this study. Section 3 covers the analysis of these data and concludes with determining properties of the planetary system and its host star. In Section 4 we discuss implications of our findings and put TIC 237913194b in context with the known exoplanet population. Finally, in Section 5 we summarize the results of our study.

We make the code used in the analysis that led to our results available in a public git repository¹.

2. OBSERVATIONS

2.1. *TESS* photometry

For identifying warm Jupiter candidates, we generated light curves for all bright stars of the TICv8 catalog from the Full Frame Images (FFIs, Jenkins et al. 2016) of *TESS* using the *tesseract*² package (Rojas, in prep.). Briefly, *tesseract* receives any TIC ID or coordinate as input and performs simple aperture photometry on the FFIs via the *TESSCut* (Brasseur et al. 2019) and *lightkurve* (Lightkurve Collaboration et al. 2018) packages. Aperture selection was done following Lund et al. (2015). Specifically, 293253 and 479184 light curves of bright objects ($T < 14$ mag) have been generated from Sectors 1 and 2, respectively. For identifying warm Jupiter candidates, we apply a simple algorithm that goes through the light curve searching for zones that significantly deviate in the negative direction from the median flux around a given region. Then we check by visual inspection if these zones are consistent with a transit-like feature. This procedure allows us in principle to identify also single transits in a given *TESS* Sector (e.g., Gill et al. 2020). By using this algorithm we found that the star TIC 237913194 presented transit-like periodic features in the two first Sectors of *TESS*. An initial fit to the photometric data indicated a period of $P \approx 15.17$ and a transit depth of $\delta_{\text{TESS}} \approx 0.8\%$, consistent with the properties of a warm giant candidate given the parameters of the star according to the TICv8 catalog. The *TESS* light curve of TIC 237913194 is shown in the upper panel of Fig. 1.

2.2. Photometric follow-up with *CHAT*

Due to the limited angular resolution of *TESS*, ground-based photometry is required to reject false positive scenarios like blended eclipsing binaries. TIC 237913194 was observed on the night of December 12, 2019 with the 0.7m Chilean-Hungarian Automated Telescope³ (*CHAT*) installed at the Las Campanas Observatory. Observations were performed with a Sloan *i'* photometric filter using a mild defocus and exposure times of 110 sec. We processed the data with a dedicated pipeline developed to produce high precision light curves using differential photometry (e.g. Espinoza et al.

¹ <https://github.com/matsicke/eccentricWarmJupiter>

² <https://github.com/astrofelipe/tesseract>

³ https://www.exoplanetscience2.org/sites/default/files/submission-attachments/poster_aj.pdf

2019b; Jones et al. 2019) with the LCOGT 1.0m telescopes (Brown et al. 2013). The optimal photometric precision was obtained with an aperture of 14 pixels (8.3"). We plot the obtained light curve in the bottom right panel of Fig. 1. We recovered a full transit, which confirms that the transit-like features identified in the *TESS* data occur in TIC 237913194. The transit depth of $\delta_{\text{CHAT}} = 0.0087 \pm 0.0004$ is consistent with the signal identified in the *TESS* photometry.

2.3. Additional photometry from LCOGT

Because of a rather grazing transit configuration, the posterior probability densities from our initial fits contained a strong degeneracy between the scaled planetary radius R_P/R_* and the impact parameter b . To lift this degeneracy and to improve the constraint on the planet radius, we obtained additional transit photometry with the Las Cumbres Observatory Global Telescope (*LCOGT*) Network on July 16, 2020 (see Fig. 1). The measurements were taken in the i' band and cover all phases of the transit. To maximize photometric precision, we chose an aperture of 24 pixels (9.4"). We recover a transit depth of $\delta_{\text{LCOGT}} = 0.0083 \pm 0.0002$. Within the uncertainties, this is consistent with the values obtained for the other instruments. Including the additional data in the fit leaves only little residual correlation between R_P/R_* and b and strongly improved the posterior on R_P (see Sect. 3.2.4).

We make all our follow-up light curves available on exoFOP⁴.

2.4. High precision spectroscopy with FEROS

We obtained high-resolution ($R = 48000$) spectra with the Fiber-fed Extended Range Optical Spectrograph (FEROS, Kaufer et al. 1999), mounted at the 2.2 m MPG telescope at La Silla Observatory. In total, 25 exposures of 1200 s were taken between June 19, 2019 and March 9, 2020. From these, we extracted radial velocities (RV) using the CERES pipeline (Brahm et al. 2017a), which performs all steps from bias, dark, and flat-field calibration to cross-correlation matching of the resulting spectrum with a G2-type binary mask. The observations were performed in the simultaneous calibration mode for tracking the instrumental velocity drift produced by changes in the spectrograph environment. This procedure involves the monitoring of a ThAr spectrum with a second fiber. The typical signal-to-noise ratio of these spectra was about 70. The time series of FEROS RV measurements is shown in Fig. 2 and they are listed in Table 6.

2.5. Contamination

We checked for possible closeby sources that could contaminate our photometric aperture with their light. Any sources within $\sim 10''$, which is the photometric aperture we used for our *LCOGT* photometry, could cause such contamination. After querying the GAIA DR2 catalog (Gaia Collaboration et al. 2018) we found the closest source to TIC 237913194 at an angular separation of $\sim 46''$. We thus find no evidence for significant contamination of our photometry.

3. ANALYSIS

3.1. Stellar Parameters

For characterizing the host star, we first determined its atmospheric parameters from the co-added FEROS spectra. Specifically, we used the ZASPE code (Brahm et al. 2017b) which compares the observed spectrum against a grid of synthetic ones generated from the ATLAS9 model atmospheres (Castelli & Kurucz 2004). We then used the PARSEC evolutionary models (Bressan et al. 2012), as described in Brahm et al. (2019), to determine the physical parameters of the star. Briefly, we compared the observed broad band photometric magnitudes of the star with those generated with models having different physical parameters by taking into account the distance determined from the Gaia DR2 parallax and assuming an extinction law of Cardelli et al. (1989) dependent on the A_V parameter. The parameter space was explored using the emcee (Foreman-Mackey et al. 2013) package. The obtained atmospheric and physical parameters of TIC 237913194 are listed in Table 1. TIC 237913194 is a main sequence G-type star with a mass of $M_* = 1.026^{+0.057}_{-0.055} M_\odot$, a radius of $R_* = 1.088^{+0.012}_{-0.012} R_\odot$, and an age of 5.7 ± 1.7 Gyr. TIC 237913194 is slightly metal rich ($[\text{Fe}/\text{H}] = +0.14 \pm 0.05$ dex) and has an effective temperature of $T_{\text{eff}} = 5788 \pm 80$ K. We note that the quoted uncertainties do not account for possible systematic errors in the stellar evolutionary models.

3.2. Joint modeling

For the joint photometry and RV modeling, we employed the python package juliet (Espinoza et al. 2019a). This tool uses existing codes to model transit photometry (batman, Kreidberg 2015) and radial velocity time series (radvel, Fulton et al. 2018). It further allows us to incorporate Gaussian Process Regression (GP) via the celerite package (Foreman-Mackey et al. 2017), which we employ to model systematic nuisance signals. To explore the parameter space, it uses the MultiNest nested sampling technique (Feroz et al. 2009), implemented in the pyMultiNest software pack-

⁴ <https://exofop.ipac.caltech.edu/teess>

age (Buchner et al. 2014). `juliet` further calculates evidences $Z_i = P(M_i(\theta)|\mathcal{D})$ for models M_i with sets of parameters θ given the data \mathcal{D} . To compare two models M_i, M_j , we compute the differences of their log-evidences,

$$\Delta \ln Z_{i,j} = \ln Z_i / Z_j = \ln [P(M_i(\theta)|\mathcal{D}) / P(M_j(\theta)|\mathcal{D})]. \quad (1)$$

Here, we adopted a general rule of thumb that if $\Delta \ln Z_{i,j} \geq 3$, the model with the larger log-evidence is favored. If $\Delta \ln Z_{i,j} \lesssim 3$, we consider the models to be indistinguishable and prefer the simpler one. As the MultiNest algorithm is known for showing scatter in $\ln Z$ that exceeds the reported uncertainties (e.g., Nelson et al. 2020), we always repeated the calculations several times. The variations among such runs were al-

ways smaller than one and therefore negligible for our purposes.

3.2.1. Model parameters

For several inferred quantities, we fitted parametrizations that allow for efficient sampling and are limited to physically plausible values:

- **Limb darkening coefficients:** to ensure uniform sampling of only physical solutions, we used a triangular sampling scheme. As outlined in Kipping (2013), we transformed the quadratic limb darkening coefficients u_1, u_2 to $q_1 = (u_1 + u_2)^2$ and $q_2 = 0.5u_1(u_1 + u_2)^{-1}$. For ground-based photometry, we assumed a linear limb darkening profile and $q_1 = u_1$.
- **Prior for the stellar density ρ_\star :** from our stellar modeling (Sect. 3.1), we obtained a distribution for the stellar density ρ_\star which we used as a prior for our joint fit instead of the scaled semi-major axis of the planetary orbit.
- **Eccentricity and argument of periastron:** we parameterized the orbital eccentricity e and the argument of periastron ω as $\mathcal{S}_1 = \sqrt{e} \sin \omega$ and $\mathcal{S}_2 = \sqrt{e} \cos \omega$ and ensure at each iteration that $e = \mathcal{S}_1^2 + \mathcal{S}_2^2 \leq 1$.

Given the observed RV variations and empirical mass-radius relationships (e.g., Chen & Kipping 2016; Neil & Rogers 2020), it is justified to neglect extreme radius ratios. We thus constrained the sampling to $R_P/R_\star < 0.5$.

3.2.2. Limb darkening

The limb darkening profile of TIC 237913194 is poorly constrained by our available data; we therefore simultaneously fit for it in the joint fit. An optimal choice of a limb darkening law is not straight-forward: there is a trade-off between accuracy and computational cost, and the performances of different laws depend on the noise level of the light curve (see Schlecker (2016) for a more detailed discussion). To account for the different noise levels in space-based and ground-based photometry (Espinoza & Jordán 2016), we decided to use a quadratic limb darkening law for *TESS* photometry and a linear law for the *CHAT* and *LCOGT* light curves.

3.2.3. RV analysis

The RV time series show a strong signal with a period corresponding to the candidate transiting planet ($P = 15.17$ d, see Fig. 2, Fig. 3). To assess the evidence of this signal being of planetary origin, we compared models

Table 1. Stellar properties of TIC 237913194

Parameter	Value	Reference
Names	TIC 237913194	<i>TESS</i>
	2MASS J01294694-6044238	2MASS
	UCAC4 147-001388	UCAC 4
RA (J2015.5)	01h29m46.99s	GAIA
DEC ... (J2015.5)	-60d44m23.67s	GAIA
pm ^{RA} (mas yr ⁻¹)	18.053 ± 0.036	GAIA
pm ^{DEC} (mas yr ⁻¹)	10.523 ± 0.034	GAIA
π (mas)	3.23 ± 0.02	GAIA
T (mag)	11.486 ± 0.006	<i>TESS</i>
B (mag)	12.746 ± 0.015	APASS
V (mag)	12.144 ± 0.069	APASS
J (mag)	10.858 ± 0.023	2MASS
H (mag)	10.571 ± 0.024	2MASS
K _s (mag)	10.485 ± 0.021	2MASS
WISE1 (mag)	10.463 ± 0.023	WISE
WISE2 (mag)	10.518 ± 0.021	WISE
WISE3 (mag)	10.408 ± 0.059	WISE
T_{eff} (K)	5788 ± 80	this work
log g (dex)	4.376 ± 0.021	this work
[Fe/H] (dex)	+0.14 ± 0.05	this work
$v \sin i$ (km s ⁻¹)	2.18 ± 0.41	this work
M_\star (M _☉)	1.026 ^{+0.057} _{-0.055}	this work
R_\star (R _☉)	1.088 ^{+0.012} _{-0.012}	this work
L_\star (L _☉)	1.196 ± 0.050	this work
Age (Gyr)	5.7 ± 1.7	this work
A _V (mag)	0.117 ^{+0.068} _{-0.063}	this work
ρ_\star (g cm ⁻³)	1.12 ± 0.11	this work

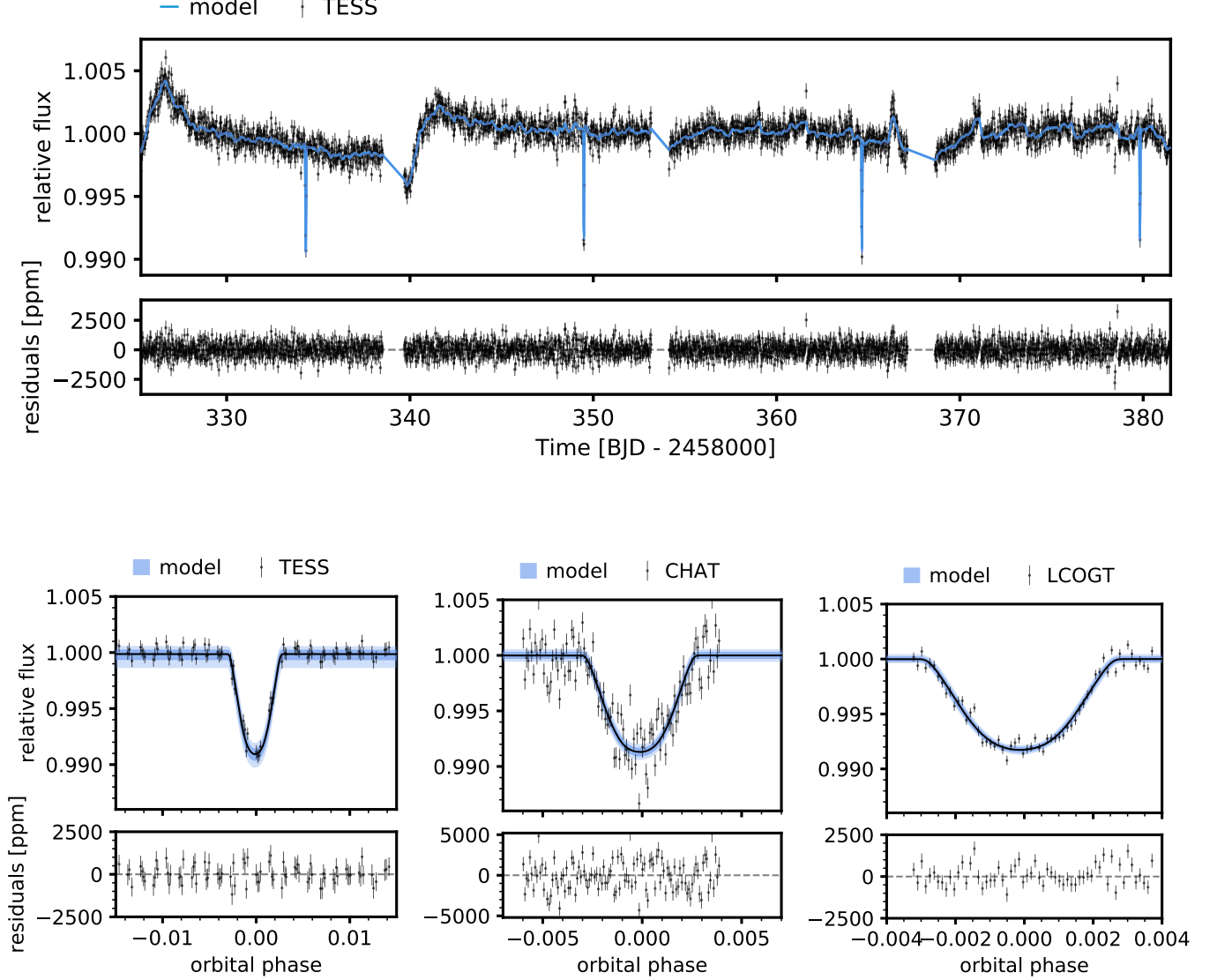


Figure 1. Photometry for TIC 237913194. Gray points represent the relative flux and errors. Solid lines show the theoretical light curve using the best-fit parameters derived in the joint modeling including GP. Blue shaded regions denote the 68 % and 95 % credibility bands of the model. Residuals are shown below each light curve. *Top:* Full *TESS* light curve generated from 30-minute-cadence photometry of Sectors 1 and 2. *Bottom left:* Phase-folded *TESS* photometry around the transit events. *Bottom center:* Follow-up photometry of a single transit obtained with *CHAT* in the i' band. *Bottom right:* *LCOGT* photometry of a single transit (i' band). This additional transit photometry lifted the $R_P/R_\star - b$ degeneracy and strongly improved our constraint on the planet radius.

with and without a planet based on only the FEROS RV dataset. We further evaluated models including more than one planet and compared the log-evidences of the different cases:

1. **No planet:** we assumed that all RV variations are due to astronomical and instrumental “jitter”. The only free parameters were μ_{FEROS} and σ_{FEROS} using the same prior distributions as in

Table 4. This “flat” model resulted in a log-evidence $\ln(Z) = -161$.

2. **Single planet:** we assumed there is a planetary signal in the RV data and widened the orbital period prior to a uniform distribution of 1-30 d. The RV semi-amplitude K was free to vary between zero and 1000 m s^{-1} (uniform prior). For T_0 , we chose a uniform prior ranging from the first pho-

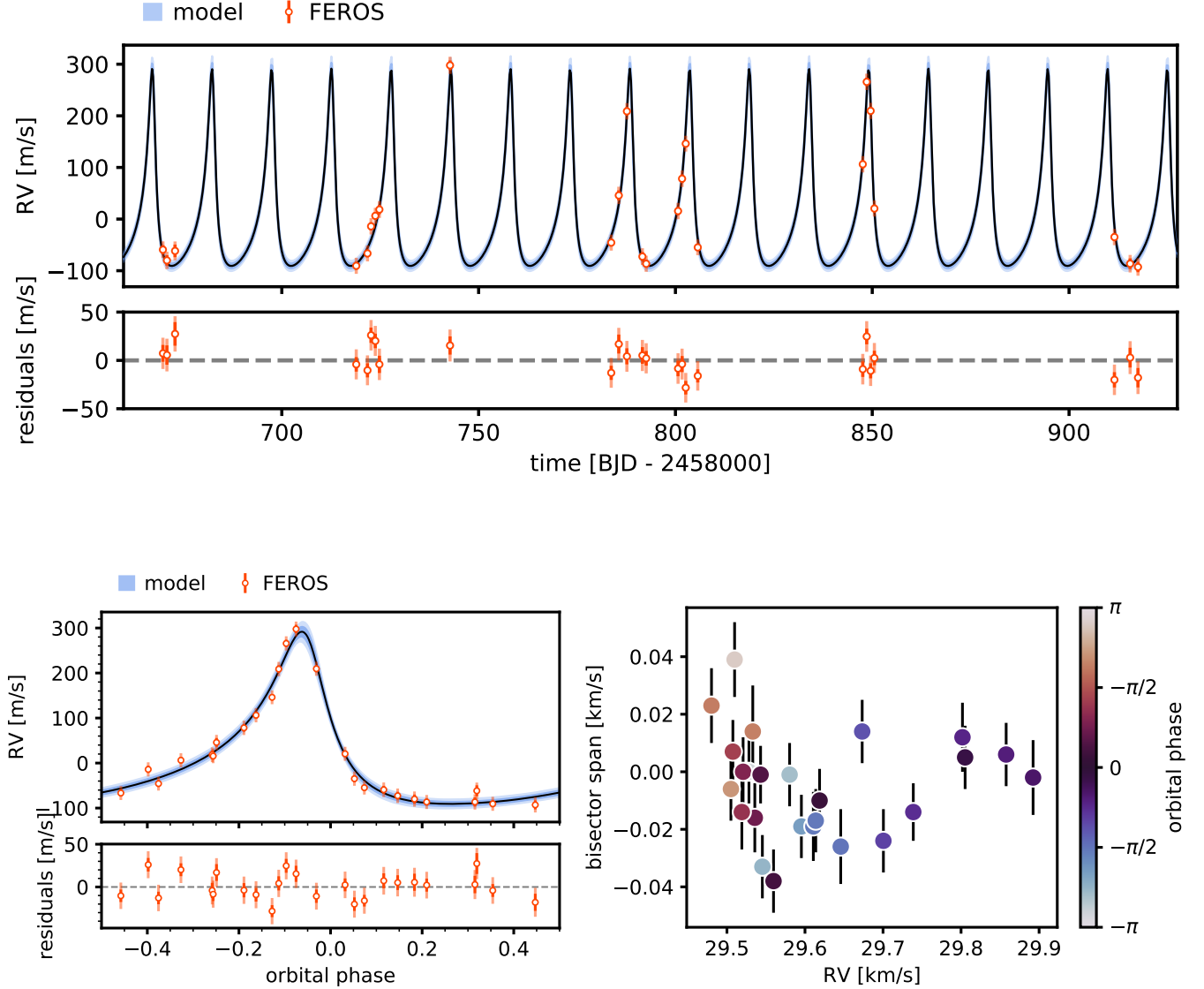


Figure 2. Radial velocity time series for TIC 237913194. Light error bars reveal the best-fit jitter term, which we added in quadrature to the RV errors. The model generated with the derived parameters of our joint modeling is plotted with a black line, and blue bands denote its 68% and 95% posterior credibility intervals. Residuals are obtained by subtracting the median posterior model from the data. *Top:* RV time series measured with the FEROS spectrograph. *Left:* phase-folded RV measurements obtained with FEROS. *Right:* bisector span as a function of radial velocity. The color of each measurement represents the orbital phase at which it was taken, assuming our best-fit period.

tometric observation to 124 d later, which corresponds to half the RV baseline. All other free parameters had the same priors as in our nominal model. This fit converged to a similar solution as our final model with a period distribution consistent with the intervals between the observed transit events. $\ln(Z) = -135$.

3. **Single planet, circular orbit:** same as 2., but fixing the eccentricity to zero (and ω to an arbitrary

90°). The fit converged to a solution with P similar to the period distribution in our final joint fit, but the jitter term is strongly increased to account for the large RV variations. With $\ln(Z) = -160$, the evidence of this model is similar to the one belonging to the no-planet hypothesis.

4. **Two planets, circular orbits:** same as 3., but assuming a second planet in the system. For this hypothetical additional planet, we let the or-

bital period vary within 1-30 d and used the same uniform prior $\mathcal{U}(0, 1000) \text{ m s}^{-1}$ for its RV semi-amplitude K_2 . The $\sim 15 \text{ d}$ periodicity is recovered, but no stable solution in favor of a two-planet-scenario is evident. $\ln(Z) = -164$

5. **Two planets, circular and eccentric orbits:** same as 4., but one planet with freely varying eccentricity. The eccentric, 15 d candidate signal is recovered. The period and RV semi-amplitude of the second planet are poorly constrained. $\ln(Z) = -151$
6. **Two planets, both on eccentric orbits:** same as 4., but with free eccentricity for both planets. Again, the 15 d signal is strongly recovered, while the weak signal of an additional planet is poorly constrained. $\ln(Z) = -144$

We list all model evidences in Table 2. The log-evidence difference between the preferred model (2. Single planet) and the runner-up (6. Two planets, both on eccentric orbits) $\Delta \ln Z_{6,2} \approx 9$, which corresponds to a Bayes factor of $\sim 10^4$. The difference to the flat model is as large as $\Delta \ln Z_{1,2} \approx 26$, implying a Bayes factor of $\sim 10^{11}$. Thus, the planetary model is strongly favored above the flat model and an eccentric single-planet solution is preferred.

To test if the candidate signal could potentially be associated with stellar activity, we produced generalized Lomb-Scargle periodograms (Zechmeister & Kürster 2009) for the radial velocity time series, as well as for common activity indicators based on FEROS data (Fig. 3). In particular, we obtained the H_α , $\log(R'_{HK})$, Na II, and He I activity indices, which trace chromospheric activity. We computed H_α following Boisse et al. (2009). As TIC 237913194 is a G-type star, we used the regions defined by Duncan et al. (1991) and the calibrations of Noyes et al. (1984) for $\log(R'_{HK})$. For Na II and He I we followed Gomes da Silva et al. (2011). For each time series (RV, H_α , $\log(R'_{HK})$, Na II, and He I), we computed the power levels for 1%, 0.5%, and 0.01% false alarm probabilities (FAP) by a bootstrap method and plot them as solid, dashed, and dotted lines, respectively. There is a strong signal in the periodogram of the radial velocities at the 15.17d period, below 0.5% FAP. Meanwhile, there are no significant signals visible in the periodograms of any of the activity indices, indicating that the radial velocity signal is unlikely to come from quasi-periodic stellar activity.

To further show beyond doubt that the measured radial velocity variations represent reflex motions of the star, we also tested if they can be caused by variations in the stellar photosphere. A well-established method

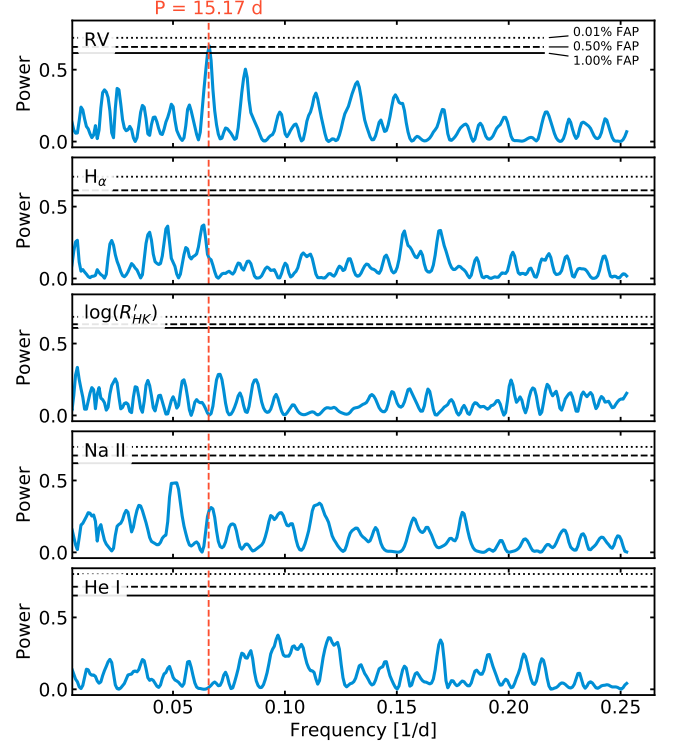


Figure 3. Generalized Lomb-Scargle periodograms of radial velocity time series and common activity indicators. Solid, dashed, and dotted lines mark 1%, 0.5%, and 0.01% false alarm probabilities, which we computed via bootstrap resamplings. The orange line marks the orbital period of TIC 237913194b.

to do this is the inspection of atmospheric line profiles, which should be constant in time for actual stellar velocity changes. Specifically, the bisector span (BIS) can serve as a diagnostic to search for possible false positive scenarios (e.g., Queloz et al. 2001). We are interested in its correlation with the RV time series and orbital phase, and confront these variables in the right panel of Fig. 2. Here, we plot the FEROS RV measurements against their bisector spans. The points are color-coded by the orbital phase of the measurements, where zero phase is at $T_0 + nP$ using median values from our nominal fit. While bisector span and RV show no evidence for correlation, this may not be true for bisector span and orbital phase. A Spearman’s rank coefficient of $0.45^{+0.31}_{-0.39}$, where we quote 95% confidence intervals from a bootstrapped sampling method⁵, permits the suspicion of a positive correlation. However, due to the small number of data points we cannot reject the null hypothesis that there is no monotonic association between the two variables.

⁵ `pingouin.compute_bootci` from the Pingouin python package (Vallat 2018)

In addition, the bisector span variations are on the order of 10 m s^{-1} and cannot account for the observed RV semi-amplitude of $K \approx 191 \text{ m s}^{-1}$. The line profiles thus provide further evidence that the observed RV variations are indeed due to velocity changes of the target star and not caused by atmospheric variations.

In addition to the tests described above, the non-sinusoidal pattern of the RVs is a strong indication for orbital motion as opposed to stellar activity. We conclude that the radial velocity time series independently confirms the planet hypothesis. In the following, we refer to the confirmed exoplanet as TIC 237913194b.⁶

3.2.4. Joint photometry and RV fit

We performed a simultaneous fit on photometric and spectroscopic datasets (*TESS*, *CHAT*, *LCOGT*, and *FEROS*) to jointly constrain all planetary parameters of TIC 237913194b. To account for the long cadence in the *TESS* light curve, we modeled the transits with 20-fold supersampling using the exposure time of the actual observations. The initial photometric fit (see Sect. 2.1) provided narrow constraints on the orbital period P and time of mid-transit T_0 . We used the median values obtained there to construct Gaussian priors for these parameters, but we enlarged the dispersions (compare Table 4). For the instrument-specific flux offsets M_{TESS} , M_{CHAT} , and M_{LCOGT} we assumed Gaussian priors based on our photometric fit. A Gaussian prior on the stellar density was motivated by the analysis of the stellar parameters presented in Sect. 3.1. Additional confidence for this prior stems from a separate joint fit where we used an uninformative prior ($\mathcal{J}(10^2, (10^4)^2)$) on ρ_* . The resulting posterior probability, $\rho_* = 996^{+257}_{-421}$, and the result from our stellar analysis agree within the uncertainties. For all other parameters, we chose uninformative priors to sample the whole physically plausible parameter space.

There are potentially time-correlated processes such as instrumental red noise, stellar variability, or blended sources that are not covered by our astrophysical model. We account for this red noise by adding a Gaussian Process (GP) component to the *TESS* photometry with an exponential kernel as implemented in the *celerite* software package (Foreman-Mackey et al. 2017). This adds two additional hyperparameters: an amplitude $\sigma_{\text{TESS}}^{\text{GP}}$ and a timescale $\tau_{\text{TESS}}^{\text{GP}}$. For comparison, we performed the same fit with and without a GP component. The variant including GP performed significantly better than

the white-noise model and we thus consider it our nominal model.

In the same manner, we tested adding a GP component to the *LCOGT* photometry, which shows possible systematic effects in the residuals (compare Fig. 1). Here, we chose a Matérn 3/2 kernel, which again adds two hyperparameters for timescale and amplitude to the model. The model including the GP component consistently performed comparable ($|\Delta \ln Z| < 1$) or worse than the model without, which is why we chose to continue with the less complex noise model without GP.

Figures 1 and 2 show the photometric and radial velocity time series resulting from this model using its median parameters (solid lines). Dark (light) blue bands show the 68 % (95 %) credibility bands of the model. The residuals below the time series show the measured data with the median posterior model subtracted; both RV and photometry residuals appear inconspicuous. Figure 4 shows the posterior distributions for the planet’s main parameters as sampled in our nominal fit. All distributions are approximately Gaussian and barely correlated, except for the planet-to-star ratio R_{P}/R_* (see Appendix A for a discussion). We present the posterior distributions of the model parameters alongside the derived physical parameters in Table 5, where we state for each parameter distribution the 16th, 50th, and 84th percentile. Notably, with a planetary bulk density $\rho_{\text{P}} \approx 1847 \text{ kg m}^{-3}$, TIC 237913194b’s average density is comparable to Neptune’s. By sheer coincidence, the planet’s period and eccentricity resemble that of the *TESS* spacecraft (13.7 d, $e = 0.55$) (Ricker et al. 2014).

3.2.5. Search for additional planets

We repeated the joint fit with an additional linear RV term to search for any long-period companions that would locally cause a linear trend in the RVs. To this end, we include intercept and slope parameters with wide, normal priors for another joint fit. The result is consistent with an RV slope of zero and the log-likelihood of the model including the linear trend is suppressed with $\Delta \ln Z \approx 7$. We conclude that the data at hand does not support additional outer companions in the system.

There is also no evidence of interior planets, which is expected since the deep intrusion of TIC 237913194b into the inner system leaves only limited room for stable inner orbits (e.g., Gladman 1993). In fact, planets like TIC 237913194b have been suggested to be a main cause for the destruction of inner systems of low-mass planets (Schlecker et al. 2020).

3.3. Approximation of the planetary equilibrium temperature

⁶ We submitted the object to exoFOP as a community *TESS* Object of Interest (CTOI); it is now listed as TOI 2179.01.

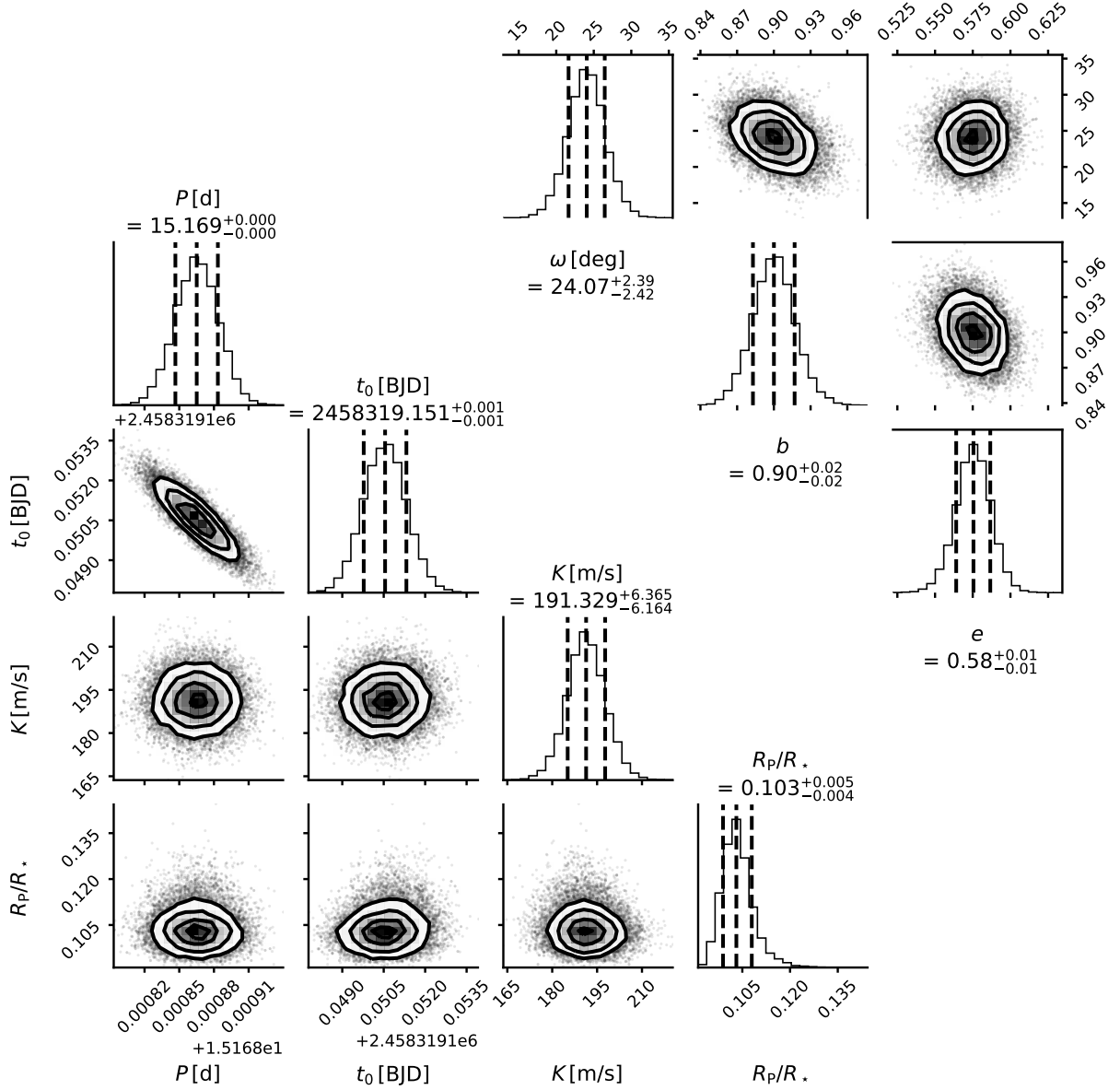


Figure 4. Posterior distributions of planetary parameters. The lower left triangle shows fitting parameters and the upper right triangle shows derived parameters of TIC 237913194b’s orbit. The stated values represent 16th, 50th, and 84th percentiles. See Appendix A for the full sample and a discussion about correlated parameters.

The equilibrium temperature T_{eq} that the planet maintains if it is in energy balance with the radiation input from the host star is a determining factor for the physical properties of its atmosphere. Due to TIC 237913194b’s considerable eccentricity, this input is not constant over its orbit. To give a first-order estimate on the temperature range that the planet can assume, we investigated two extreme cases of planetary heat adjustment:

1. instantaneous heat adjustment ($T_{\text{eq,inst}}$). Here, we assumed that the planetary atmosphere adjusts to

the changing irradiation without any time delay. For this situation, we used the approximation in [Kaltenegger & Sasselov \(2011, Equation 3\)](#).

2. orbitally averaged heat adjustment ($T_{\text{eq,avg}}$). In this case, the planetary temperature remains in equilibrium with the incoming stellar energy, i.e. $T_{\text{eq}} = \text{const.}$ over one orbit. To approximate this temperature, we used a temporal average for elliptic orbits ([Méndez & Rivera-Valentín 2017, Equation 16](#)).

For both extremes, we assumed that the heat flux from the planet’s interior is negligible compared to the stellar irradiation and ignored any internal energy sources. The infrared emissivity ε_{IR} was fixed to unity. We further assumed two cases for how atmospheric flow distributes the incoming stellar energy over the planetary surface and parametrized this property with the fraction of planetary surface that re-radiates stellar flux β . We distinguished between $\beta = 0.5$, i.e. emission only from one hot hemisphere, and $\beta = 1$ where the whole globe emits (Seager et al. 2005; Kaltenegger & Sasselov 2011; Carone et al. 2014; Méndez & Rivera-Valentín 2017).

Planets colder than 1000 K are expected to be relatively cloudy (e.g., Stevenson 2016; Parmentier et al. 2016). Here, we parametrized different cloudiness with albedos $\alpha = 0, 0.3$, and 0.6 following Parmentier et al. (2016). With the above assumptions and in the case of instantaneous heat adjustment, we derived a range of $T_{\text{eq,inst}} \approx 900 - 1300$ K at secondary eclipse and $T_{\text{eq,inst}} \approx 700 - 1100$ K at transit (Fig. 5). We list $T_{\text{eq,inst}}$ at critical times in Table 3 together with the values for orbitally averaged heat adjustment $T_{\text{eq,avg}}$. The latter is constant over one orbit and covers a temperature range of $T_{\text{eq,avg}} \approx 650 - 975$ K.

Due to the orientation of the orbit (compare Fig. 6), the temperature $T_{\text{eq,inst}}$ during transit is assumed to be about 200 K colder compared to the temperature at secondary eclipse. In reality, however, some delay in heat adjustment based on radiative and dynamical timescales is expected. Therefore, the temperature during a secondary eclipse, which would occur before passage of periastron, could be colder than in our estimate. Likewise, the temperature at transit, occurring after periastron passage, would be warmer than expected (see, e.g., Lewis et al. 2013, for a qualitative discussion of the thermal evolution of an exoplanet on an eccentric orbit).

Table 2. Model evidences from RV fits for different models. $\Delta \ln Z$ states the difference in log-evidence compared to our best model “1 planet, eccentric orbit”.

Model	log-evidence $\ln Z$	$\Delta \ln Z$
0 planets	-160.94 ± 0.14	-26.41
1 planet, eccentric orbit	-134.53 ± 0.02	0
1 planet, circular orbits	-160.46 ± 0.04	-25.93
2 planets, circular orbits	-164.34 ± 0.02	-29.81
2 planets, circular&eccentric orbits	-150.76 ± 0.01	-16.23
2 planets, eccentric orbits	-144.46 ± 0.01	-9.93

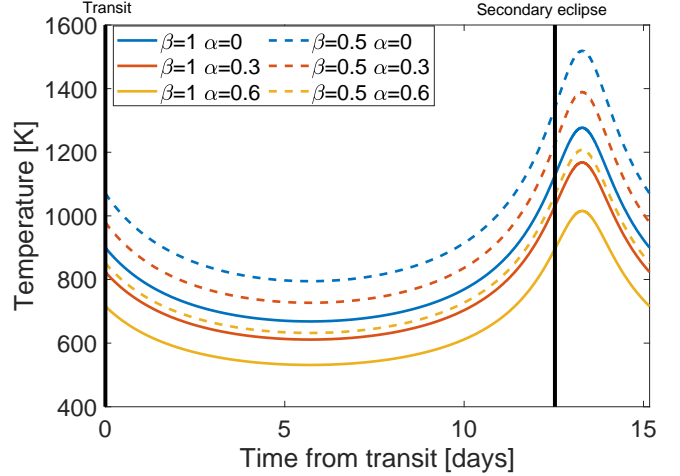


Figure 5. Evolution of the planetary equilibrium temperature in the case of instantaneous heat adjustment for different albedos α and re-radiation factors β . We assumed unity infrared emissivity ε_{IR} . Black lines denote the time of transit and secondary eclipse, respectively. Due to the high eccentricity, $T_{\text{eq,inst}}$ varies by several hundred Kelvin within one orbit. It stays below 1000 K for most of the orbit.

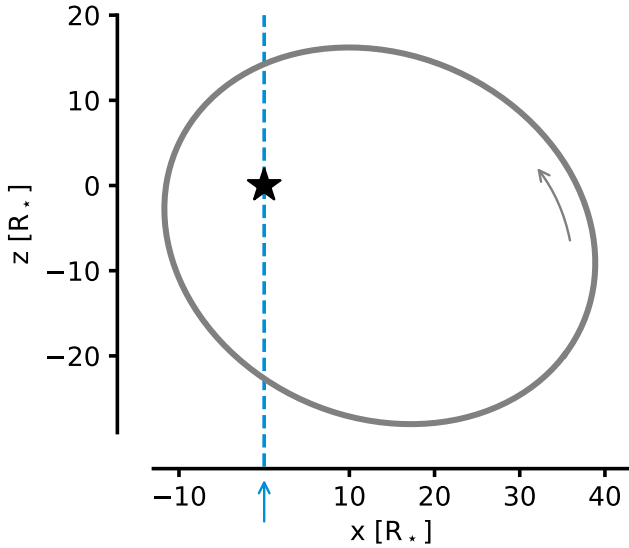
We emphasize again that our goal is to estimate to first order possible temperature ranges for TIC 237913194b for which these simplified assumptions are sufficient.

3.4. Secondary eclipses, phase curve modulations, and Rossiter-MacLaughlin effect

No secondary eclipses or phase curve signals are evident in the photometric time series. We used the *starry* software package (Luger et al. 2019) to estimate the planetary phase curve based on our derived orbital parameters and a simple toy model for the planetary brightness distribution. This model neglects any heat redistribution between the hot and cold hemispheres of the planet, resulting in a ‘dipole’ brightness map where the hot side points to the substellar point at periastron. In this scenario, the emission of the cold hemisphere and planetary limb darkening are negligible. The total luminosity of the planet is then that of a half-sphere black body with radius R_{P} and temperature T_{hot} . For the temperature of the hot hemisphere, we adopt two cases: firstly, our estimate of the equilibrium temperature for the case of orbitally averaged heat adjustment and $\beta = 0.5$, hence $T_{\text{hot}} = T_{\text{eq,avg}} = 974$ K. Secondly, we consider the hottest temperature in Table 3 and assume $T_{\text{hot}} = 1519$ K. With a resulting peak-to-peak phase curve amplitude of ~ 6 ppm in the cool case and ~ 32 ppm in the hot case, a future detection of the phase curve or secondary eclipse might be challenging despite the expected precision of the James Webb Space Telescope (JWST, Beichman et al. 2014).

Table 3. Theoretical temperature constraints of TIC 237913194b in the course of one orbit.

Time	orbital distance	$T_{\text{eq,inst}}$ [K]			$T_{\text{eq,avg}}$ [K]		
	[au]	$\alpha = 0$	$\alpha = 0.3$	$\alpha = 0.6$	$\alpha = 0$	$\alpha = 0.3$	$\alpha = 0.6$
$\beta = 1$							
apoastron	0.1900	668	611	531			
transit	0.1047	900	823	716	819	749	651
periastron	0.0520	1277	1168	1016			
secondary eclipse	0.0668	1127	1031	896			
$\beta = 0.5$							
apoastron	0.1900	795	727	632			
transit	0.1047	1070	979	851	974	891	775
periastron	0.0520	1519	1389	1208			
secondary eclipse	0.0668	1340	1226	1066			

**Figure 6.** Orbit aspect ratio and orientation. The orbit of TIC 237913194b is plotted with stellar radii as length units. The dashed blue line shows our line of sight with respect to the orbit.

Measuring the Rossiter-McLaughlin effect (RM effect, Rossiter 1924; McLaughlin 1924) has proved a useful tool to measure the alignment of planetary orbits with the spin axis of host stars. The different proposed scenarios for the formation and migration theory of warm Jupiters differ in their predicted impact on the spin-orbit alignment (e.g., Triaud 2018). A detection of the RM effect could thus shed light on TIC 237913194b’s enigmatic formation history. Analytical formulas exist to estimate the amplitude of its RV signature (e.g., Gaudi & Winn 2007, equation 6), however, the large impact parameter in TIC 237913194b’s transit geometry would entail a large error. Instead, we modeled the RV anomaly due to the Rossiter-McLaughlin effect with a velocity-weighted brightness map in *starry* using the

median posterior values of the system’s physical parameters (see Tables 1 and 5).

The resulting amplitude of the signal $K_{\text{RM}} \approx 10 \text{ ms}^{-1}$, which is just in the range of current state-of-the-art spectroscopic facilities.

4. DISCUSSION

4.1. TIC 237913194b’s place in the exoplanet population

In Fig. 7 we compare TIC 237913194b with well-studied transiting exoplanets (Southworth 2011)⁷. The left panel shows the periods and eccentricities of these planets (blue markers); our discovery is marked in red. We included planets with both mass and radius measurements that have constrained eccentricities (not only upper limits) and show those in the period range 1-100 d. Marker sizes in the plot correspond to planet masses. Warm Jupiters with high eccentricities appear to be rare: 98% of this population have smaller eccentricities than TIC 237913194b, making it one of the most eccentric planets in this period range. It lies at the edge of a demographic feature that we discuss in the following.

On close orbits, the planet occurrence rate dn/de shows a rapid drop with increasing eccentricity. With increasing period, the position of this ridge shifts to larger eccentricities. Through this, a triangular underdensity of planets with high eccentricity on very short orbits emerges (upper left corner in Fig. 7). While exoplanet detection sensitivities are expected to have a dependency on eccentricity, the effect is too small to account for the observed dearth of planets (Burke 2008). A plausible physical explanation would be tidal circularization (Adams & Laughlin 2006; Dawson & Johnson 2018). As discussed in Sect. 4.3, the strength of this

⁷ TEPcat catalog, queried on 2020-08-11.

Table 4. Prior parameter distributions.

$N(\mu, \sigma)$ stands for a normal distribution with mean μ and standard deviation σ , $U(a, b)$ stands for a uniform distribution between a and b , and $J(a, b)$ stands for a Jeffrey’s prior (that is, a log-uniform distribution) defined between a and b .

Parameter name	Prior	Units	Description
Stellar Parameters			
ρ_\star	$\mathcal{N}(1120, 110^2)$	kg/m ³	Stellar density
Planetary parameters			
P	$\mathcal{N}(15.16, 0.2^2)$	d	Period
t_0	$\mathcal{N}(2458319.17, 0.2^2)$	d	Time of transit center
R_P/R_\star	$\mathcal{U}(0.0, 1.5)$	—	Impact factor
$b = (a/R_\star) \cos(i)$	$\mathcal{U}(0.0, 0.5)$	—	Planet-to-star ratio
K	$\mathcal{U}(140.0, 260.0)$	m/s	Radial velocity semi-amplitude
$S_1 = \sqrt{e} \sin \omega$	$\mathcal{U}(-1, 1)$	—	Parametrization for e and ω
$S_2 = \sqrt{e} \cos \omega$	$\mathcal{U}(-1, 1)$	—	Parametrization for e and ω
RV instrumental parameters			
μ_{FEROS}	$\mathcal{U}(-30, 30)$	m/s	Systemic velocity for FEROS
σ_{FEROS}	$\mathcal{J}(1.0, 100.0^2)$	ppm	Extra jitter term for FEROS
$\text{RV}_{\text{linear}}$	$\mathcal{N}(0.0, 1.0^2)$	m/s/d	Linear term for the RVs ^a
$\text{RV}_{\text{intercept}}$	$\mathcal{N}(0.0, 10000^2)$	m/s	Intercept term for the RVs ^a
Photometry instrumental parameters			
D_{TESS}	1.0 (fixed)	—	Dilution factor for TESS
M_{TESS}	$\mathcal{N}(0.0, 0.1^2)$	ppm	Relative flux offset for TESS
σ_{TESS}	$\mathcal{J}(10^{-5}, (10^5)^2)$	ppm	Extra jitter term for TESS
$q_{1,\text{TESS}}$	$\mathcal{U}(0.0, 1.0)$	—	Linear limb-darkening parametrization
$q_{2,\text{TESS}}$	$\mathcal{U}(0.0, 1.0)$	—	Quadratic limb-darkening parametrization
D_{CHAT}	1.0 (fixed)	—	Dilution factor for CHAT
M_{CHAT}	$\mathcal{N}(0.0, 0.1^2)$	ppm	Relative flux offset for CHAT
σ_{CHAT}	$\mathcal{J}(10^{-5}, (10^5)^2)$	ppm	Extra jitter term for CHAT
$q_{1,\text{CHAT}}$	$\mathcal{U}(0.0, 1.0)$	—	Linear limb-darkening parametrization
D_{LCOGT}	1.0 (fixed)	—	Dilution factor for <i>LCOGT</i>
M_{LCOGT}	$\mathcal{N}(0.0, 0.1^2)$	ppm	Relative flux offset for <i>LCOGT</i>
σ_{LCOGT}	$\mathcal{J}(10^{-5}, (10^5)^2)$	ppm	Extra jitter term for <i>LCOGT</i>
$q_{1,\text{LCOGT}}$	$\mathcal{U}(0.0, 1.0)$	—	Linear limb-darkening parametrization
Additional parameters			
$\sigma_{\text{TESS}}^{\text{GP}}$	$\mathcal{J}(10^{-8}, 0.0005^2)$	—	Amplitude of the GP component
$\tau_{\text{TESS}}^{\text{GP}}$	$\mathcal{J}(0.0001, 2^2)$	—	Timescale of the GP component

^aThese parameters were only used to search for an additional linear RV trend and are not included in our nominal joint fit.

mechanism is expected to scale inversely with orbital distance, which would explain the period-dependence of the distribution. The detection of planets close to this ridge can thus help constrain theories of tidal interaction and giant planet migration, which are crucial components for explaining planetary systems with close-in giant planets. Our discovery of TIC 237913194b adds to the small current sample of such planets.

In the right panel of Fig. 7, we put our planet into context of warm Jupiters with mass and radius measurements. Here, we include only planets from TEPcat with periods of 10-100 d, and color-code them by equilibrium temperature. We further plot a theoretically predicted mass-radius relation for planets with a 10 M_\oplus core (Fortney et al. 2007, blue line). TIC 237913194b is

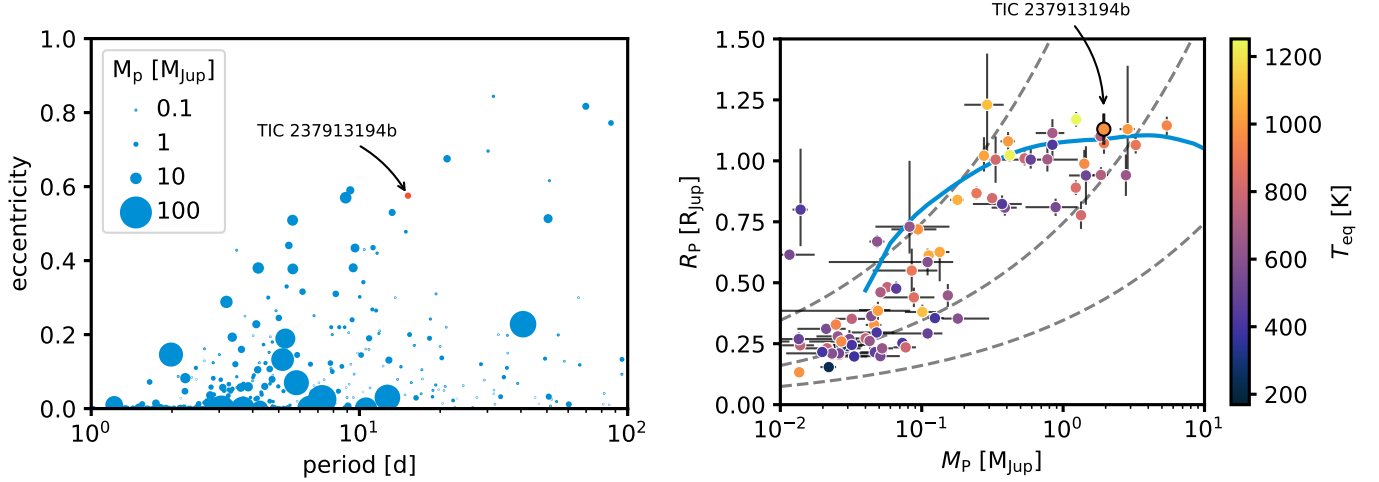


Figure 7. Comparison to other well-characterized warm Jupiters. *Left:* period-eccentricity plot of transiting exoplanets with periods of 1-100 d and measured eccentricity from the TEPcat catalog (Southworth 2011). Marker sizes scale with planet mass. With $e = 0.58$, TIC 237913194b occupies the 98th percentile in this population and contributes to a sparse sample of planets with very high eccentricities.

Right: mass-radius diagram of *warm* ($P = 10 - 100$ d) planets from the same catalog. The color of the markers represent the equilibrium temperatures of the planets, and dashed gray lines are isodensity curves of 0.3 , 3 , and 30 g cm^{-3} , respectively. The solid blue line marks the predicted mass-radius relation for giant planets with a $10 M_{\oplus}$ core (Fortney et al. 2007). TIC 237913194b lies very close to this line. The error bars for its mass are too small to be seen.

located close to this curve, which indicates that its bulk density is consistent with established structural models.

4.2. The atmosphere of TIC 237913194b

The large eccentricity of TIC 237913194b makes it a promising test bed to study the response of its atmosphere to external forcing (e.g., compare Carone et al. 2020). Atmospheres at the inferred temperature ranges are susceptible to a variety of chemical disequilibrium processes such as photochemistry and chemical quenching (e.g. Molaverdikhani et al. 2019a; Moses et al. 2013; Venot et al. 2012, 2020; Tsai et al. 2018; Kawashima & Ikoma 2019). While a thorough inspection of these processes is beyond the scope of this paper, we used the physical parameters constrained here to demonstrate the feasibility of atmospheric characterization. To this end, we used self-consistent models for cloud-free (Molaverdikhani et al. 2019b) and cloudy (Molaverdikhani et al. 2020) irradiated planetary atmospheres and calculated synthetic transmission and emission spectra using *petitCODE* (Mollière et al. 2015; Mollière et al. 2017). For this fiducial model, we assumed solar composition, zero bond albedo, instantaneous thermal equilibrium, and $\beta = 0.5$. This resulted in an equilibrium temperature of the planet during transit and secondary eclipse of 1070 K and 1340 K, respectively (see Table 3). Using the *Pandexo* package (Batalha et al.

2017), we predicted uncertainties for JWST observations of a single transit or secondary eclipse for the three observing modes MIRI-LRS, NIRISS-SOSS, and NIRSpec-G395M.

We find relative magnitudes of the largest synthetic spectral features of ~ 100 ppm in transmission and ~ 1000 ppm in emission. While some emission features are well above the predicted noise floor, the largest transmission features are on the order of the predicted uncertainties for a single transit observation. However, since these two techniques probe different regions of the atmosphere and at different orbital phases, a joint analysis of the transmission and emission spectra may provide important clues on atmospheric dynamics and heat redistribution.

4.3. TIC 237913194b’s large eccentricity

The peculiarly large eccentricity of TIC 237913194b could be an important lead in not only understanding the dynamical origin of the system, but also planet evolution theories in general. Possible origins of large warm Jupiter eccentricities include interaction with a massive companion through either scattering events (e.g., Rasio & Ford 1996), secular interactions (e.g., Petrovich & Tremaine 2016; Kozai 1962; Lidov 1962), or giant impacts (Freikh et al. 2019); planet-disk interactions (e.g., Lubow 1991; Petrovich et al. 2019); or a combination of

processes. The absence of evidence for an additional perturber that might sustainably excite TIC 237913194b's

Table 5. Posterior parameters

Parameter	Value
Stellar Parameters	
ρ_* (kg/m ³)	1076^{+95}_{-93}
Planetary parameters	
P (d)	$15.168865^{+0.000018}_{-0.000018}$
t_0 (BJD UTC)	$2458319.15055^{+0.00077}_{-0.00077}$
a/R_*	$23.85^{+0.67}_{-0.69}$
$b = (a/R_*) \cos(i)$	$0.900^{+0.017}_{-0.017}$
R_P/R_*	$0.1031^{+0.0048}_{-0.0042}$
K (m/s)	$191.3^{+6.4}_{-6.2}$
e	$0.575^{+0.011}_{-0.011}$
ω	$24.1^{+2.4}_{-2.4}$
$S_1 = \sqrt{e} \sin \omega$	$0.309^{+0.029}_{-0.030}$
$S_2 = \sqrt{e} \cos \omega$	$0.692^{+0.014}_{-0.015}$
RV instrumental parameters	
μ_{FEROS} (m/s)	$14.0^{+3.4}_{-3.3}$
σ_{FEROS} (m/s)	$13.6^{+3.2}_{-2.6}$
Photometry instrumental parameters	
M_{TESS} (ppm)	$0.00017^{+0.00041}_{-0.00039}$
σ_{TESS} (ppm)	221^{+28}_{-31}
$q_{1,\text{TESS}}$	$0.33^{+0.39}_{-0.24}$
$q_{2,\text{TESS}}$	$0.27^{+0.35}_{-0.20}$
$\sigma_{\text{TESS}}^{GP}$	$0.00000152^{+0.00000110}_{-0.00000041}$
τ_{TESS}^{GP}	$0.40^{+0.16}_{-0.18}$
M_{CHAT} (ppm)	$0.00149^{+0.00025}_{-0.00025}$
σ_{CHAT} (ppm)	1625^{+150}_{-140}
$q_{1,\text{CHAT}}$	$0.55^{+0.20}_{-0.24}$
M_{LCOGT} (ppm)	$-0.00038^{+0.00016}_{-0.00016}$
σ_{LCOGT} (ppm)	480^{+85}_{-80}
$q_{1,\text{LCOGT}}$	$0.67^{+0.17}_{-0.20}$
Derived parameters	
i (deg)	$87.0^{+1.5}_{-1.7}$
R_P [R _{Jup}]	$1.117^{+0.054}_{-0.047}$
M_P [M _{Jup}]	$1.942^{+0.092}_{-0.091}$
a [au]	$0.1207^{+0.0037}_{-0.0037}$
ρ_P [kg m ⁻³]	1847^{+280}_{-260}
T_{eq} [K] ^a	974

^aTime-averaged equilibrium temperature computed according to equation 16 of Méndez & Rivera-Valentín (2017). We assumed zero albedo, a unity broadband thermal emissivity, and $\beta = 0.5$, i.e. only half of the planetary surface re-radiates the absorbed flux.

eccentricity or that could be the counterpart in a recent scattering event makes it challenging to distinguish between these scenarios.

However, TIC 237913194b is subject to tidal dissipation through secular interaction with the host star (Goldreich & Soter 1966) and the rates of semi-major axis and eccentricity decay, given the current orbital parameters, can be estimated (Yoder & Peale 1981). A short orbit circularization timescale compared to the lifetime of the star would exclude the planet-disk interaction scenario and could provide an upper limit on the time that has passed since a hypothetical perturbation event. In this case, we would observe the system during high-eccentricity migration and TIC 237913194b would eventually become a hot Jupiter in a circular orbit.

Several caveats have to be considered when trying to trace the system back in time close to its primordial orbital configuration. First, the tidal evolution of a and e are strongly coupled, which may result in ambiguities. In addition, the tidal evolution strongly depends on the stellar and planetary tidal dissipation rates, typically parameterized by the dimensionless “reduced tidal quality factors” Q'_P and Q'_* . Here, $Q' = 1.5 Q/k_2$, where k_2 , is the Love number of second order. Estimates of the planetary tidal quality factor range from $Q'_P = 10^4$ to $Q'_P = 10^7$ (e.g. Lainey et al. 2009; Lainey et al. 2020; Hansen 2012). The stellar tidal dissipation factor is even less well constrained but theoretical and observational works suggest $Q'_* \gtrsim 10^7$ (e.g. Carone & Pätzold 2007; Hansen 2012; Damiani & Lanza 2015).

We studied the star-planet tides of TIC 237913194b using the EqTide⁸ code (Barnes 2017), which calculates the tidal evolution of two bodies based on models by Ferraz-Mello et al. (2008) and a “constant-phase-lag” (CPL) model (Goldreich & Soter 1966; Cheng et al. 2014). For our tidal-torque test, we adopted a Stellar rotational period of 30 d and an initial planetary rotational period of 0.5 d (i.e., similar to the Solar and Jupiter rotational periods). We adopted tidal quality factors Q'_P in the range of 3×10^4 - 10^6 . For the primary, we chose a fixed value of $Q'_* = 10^8$ (e.g., Hansen 2010; Penev et al. 2012; Bonomo et al. 2017). We tested a large set of increased initial semi-major axes and eccentricities and integrated with EqTide. The results agree with the observed eccentricity and semi-major axis only for those samples that started a few percent above the observed values. This suggests that the orbital period of ~ 15 d is too large for significant tidal circularization within the age of the system (~ 5.5 Gyr, see Table 1)

⁸ <https://github.com/RoryBarnes/EqTide>

and TIC 237913194b’s orbit has only slightly evolved from its primordial configuration. These results are in line with Barnes (2015), who showed that Jovians with periods longer than ~ 8 days and a typical eccentricity of 0.3 do not experience significant orbital and eccentricity decay. While we cannot determine the origin of the high orbital eccentricity, we conclude that the planet we observe today is not a credible progenitor of a future hot Jupiter.

5. CONCLUSIONS

We have presented the discovery of TIC 237913194b (TOI 2179b), a transiting warm Jupiter orbiting its G-type host in a very eccentric ($e \approx 0.58$) 15-day orbit. Its transit signal was detected using *TESS* full frame images from Sectors 1 and 2. We confirmed the planetary nature of the signal using ground-based photometry (*CHAT*, *LCOGT*) and high-precision spectroscopy (*FEROS*). Our main results are:

- a planetary mass $M_P = 1.942^{+0.091}_{-0.091} M_J$ and radius $R_P = 1.117^{+0.054}_{-0.047} R_J$, yielding a bulk density similar to Neptune’s.
- with $e \approx 0.58$ one of the highest eccentricities among all currently known warm giants.
- slow tidal evolution, prohibitive of a hot Jupiter progenitor scenario.
- an attractive opportunity for future observations of the planet’s atmosphere, which might harbor observable chemical disequilibrium processes due to the greatly varying external forcing.
- good prospects for detecting the Rossiter-MacLaughlin effect, which would be a valuable contribution to the still small sample of warm Jupiters with constrained spin-orbit obliquities.

ACKNOWLEDGMENTS

M.S. gratefully acknowledges insightful discussions with Robin Baeyens, Francesco Biscani, and Robert Glas. R.B. acknowledges support from FONDECYT Post-doctoral Fellowship Project 3180246, and from the Millennium Institute of Astrophysics (MAS). L.C. acknowledges support from the DFG Priority Programme SP1833 Grant CA 1795/3. A.J. acknowledges support from FONDECYT project 1171208, CONICYT project Basal AFB-170002, and by the Ministry for the Economy, Development, and Tourism’s Programa Iniciativa Científica Milenio through grant IC120009, awarded to the Millennium Institute of Astrophysics (MAS). T.H. and P.M. acknowledge support from the European Research Council under the Horizon 2020 Framework Program via the ERC Advanced Grant Origins 83 24 28. This work was supported by the DFG Research Unit FOR2544 “Blue Planets around Red Stars”, project no. RE 2694/4-1. This research was supported by the Deutsche Forschungsgemeinschaft through the Major Research Instrumentation Programme and Research Unit FOR2544 “Blue Planets around Red Stars” for T.H. under contract DFG He 1935/27-1 and for H.K. under contract DFG KL1469/15-1. This research has made use of the Exoplanet Follow-up Observation Program website, which is operated by the California Institute of Technology, under contract with the National Aeronautics and Space Administration under the Exoplanet Exploration Program. Funding for the *TESS* mission is provided by NASA’s Science Mission directorate. This paper includes data collected by the *TESS* mission, which are publicly available from the Mikulski Archive for Space Telescopes (MAST). Resources supporting this work were provided by the NASA High-End Computing (HEC) Program through the NASA Advanced Supercomputing (NAS) Division at Ames Research Center for the production of the SPOC data products.

Facilities: *TESS*, LCO, CHAT0.7m, LCOGT1.0m, MPG2.2m/FEROS

Software: astropy (Astropy Collaboration et al. 2013), juliet (Espinoza et al. 2019a), CERES (Brahm et al. 2017a; Jordán et al. 2014), ZASPE (Brahm et al. 2017b, 2015), tesseract (Rojas, in prep.), TESS-Cut (Brasseur et al. 2019), lightkurve (Lightkurve Collaboration et al. 2018), radvel (Fulton et al. 2018), emcee (Foreman-Mackey et al. 2013), corner.py (Foreman-Mackey 2016), MultiNest (Feroz et al. 2009), PyMultiNest (Buchner et al. 2014), batman (Kreidberg 2015), starry (Luger et al. 2019), celerite (Foreman-Mackey

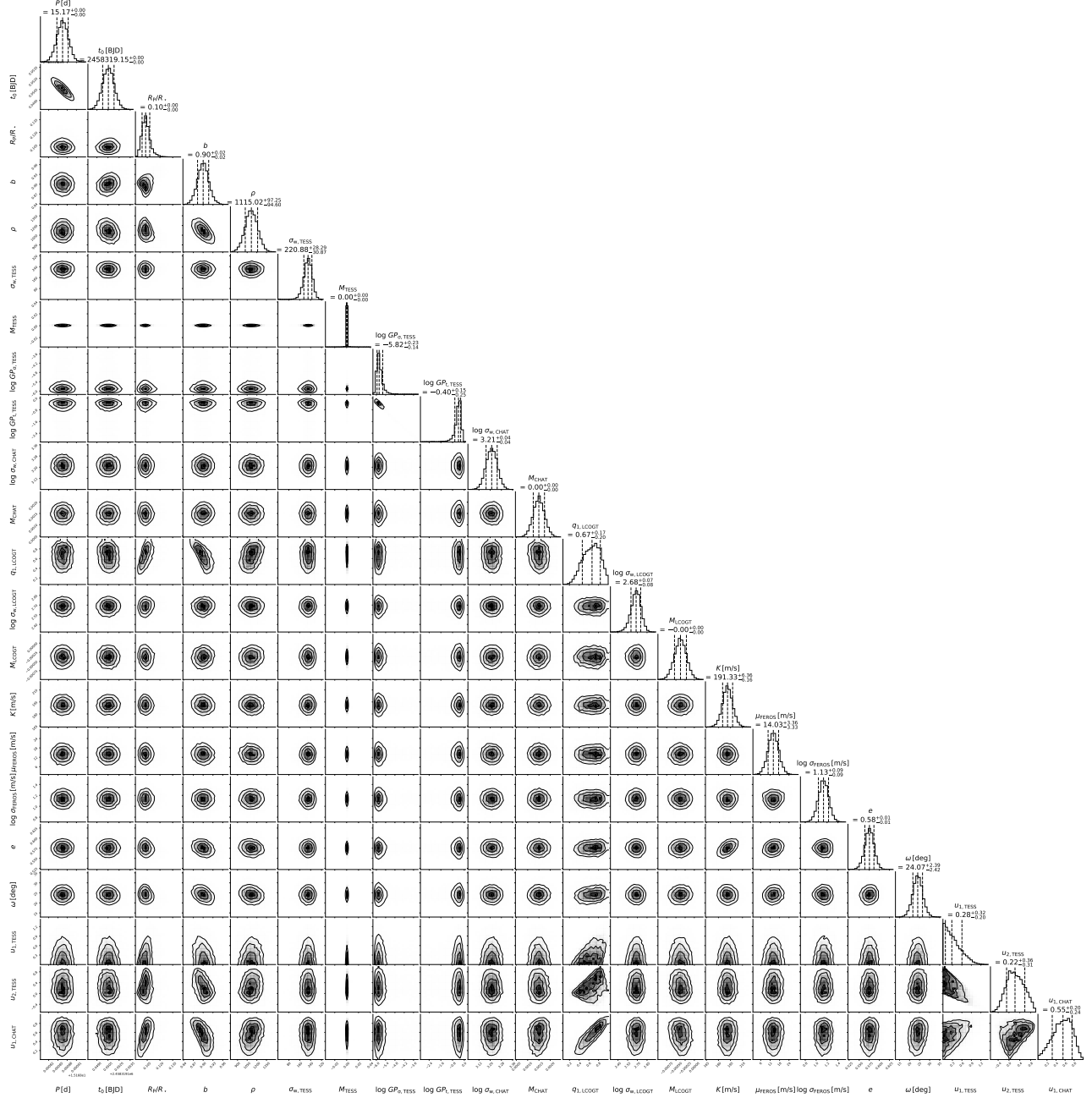


Figure 8. Corner plot showing the posteriors of all parameters in our joint fit. The stated values represent 16th, 50th, and 84th percentiles, and we consider the median our ‘best fit’. Individual sample points are not drawn to limit file size.

et al. 2017), petitCODE (Mollière et al. 2015; Mollière

et al. 2017), EqTide (Barnes 2017), Pingouin (Vallat 2018).

APPENDIX

A. JOINT FIT POSTERIOR

Figure 8 shows all combinations of one- and two-dimensional projections of the posterior space from our joint fit (see Sect. 3.2.4). On the diagonal, we state for each parameter the median value and its 16th and 84th percentile.

Table 6. FEROS radial velocities and accompanying data for TIC 237913194 used in this paper.

BJD	RV [km/s]	σ_{RV} [km/s]	t_{exp} [s]	BIS [km/s]	σ_{BIS} [km/s]
2458669.798	29.536	0.009	1200	-0.016	0.012
2458670.816	29.519	0.010	1200	-0.014	0.013
2458672.879	29.533	0.012	1200	0.014	0.016
2458718.916	29.505	0.007	1200	-0.006	0.011
2458721.768	29.528	0.007	1200	-0.000	0.011
2458722.674	29.580	0.008	1200	-0.001	0.011
2458723.758	29.595	0.007	1200	-0.019	0.011
2458724.793	29.611	0.009	1200	-0.019	0.012
2458742.740	29.892	0.009	1200	-0.002	0.013
2458783.690	29.545	0.007	1200	-0.033	0.011
2458785.610	29.646	0.010	1200	-0.026	0.013
2458787.671	29.802	0.008	1200	0.012	0.012
2458791.610	29.521	0.009	1200	-0.000	0.012
2458792.571	29.508	0.008	1200	0.007	0.011
2458800.668	29.614	0.008	1200	-0.017	0.011
2458801.688	29.673	0.008	1200	0.014	0.011
2458802.619	29.739	0.007	1200	-0.014	0.010
2458805.675	29.543	0.007	1200	-0.001	0.010
2458847.592	29.701	0.008	1200	-0.024	0.011
2458848.591	29.858	0.008	1200	0.006	0.011
2458849.592	29.805	0.008	1200	0.005	0.011
2458850.541	29.619	0.007	1200	-0.010	0.011
2458911.524	29.560	0.008	1200	-0.038	0.011
2458915.515	29.480	0.010	1200	0.023	0.013
2458917.514	29.510	0.010	1200	0.039	0.013

There is some residual degeneracy in the $b - R_P/R_\star$ plane. In previous fits that did not include *LCOGT* data, the distribution extended far into the range of large impact parameters and planet-to-star ratios, marking a degenerate solution. This effect is physically plausible: a larger planet with higher impact parameter can to some degree mimic a smaller one with lower impact parameter. In the joint fit shown in Fig. 8, this degeneracy is lifted and both b and R_P/R_\star are well constrained.

B. RV DATA

REFERENCES

- Adams, F. C., & Laughlin, G. 2006, *The Astrophysical Journal*, 649, 1004, doi: [10.1086/506145](https://doi.org/10.1086/506145)
- Astropy Collaboration, Robitaille, T., Tollerud, E., et al. 2013, *\aap*, 558, A33, doi: [10.1051/0004-6361/201322068](https://doi.org/10.1051/0004-6361/201322068)
- Barclay, T., Pepper, J., & Quintana, E. V. 2018, *The Astrophysical Journal Supplement Series*, 239, 2, doi: [10.3847/1538-4365/aac3e9](https://doi.org/10.3847/1538-4365/aac3e9)
- Barnes, R. 2015, *International Journal of Astrobiology*, 14, 321, doi: [10.1017/S1473550413000499](https://doi.org/10.1017/S1473550413000499)
- . 2017, *Celestial Mechanics and Dynamical Astronomy*, 129, 509, doi: [10.1007/s10569-017-9783-7](https://doi.org/10.1007/s10569-017-9783-7)
- Batalha, N. E., Mandell, A., Pontoppidan, K., et al. 2017, *Publications of the Astronomical Society of the Pacific*, 129, 064501
- Beichman, C., Benneke, B., Knutson, H., et al. 2014, *Publications of the Astronomical Society of the Pacific*, 126, 1134, doi: [10.1086/679566](https://doi.org/10.1086/679566)
- Boisse, I., Moutou, C., Vidal-Madjar, A., et al. 2009, *A&A*, 495, 959, doi: [10.1051/0004-6361:200810648](https://doi.org/10.1051/0004-6361:200810648)

- Bonomo, A. S., Desidera, S., Benatti, S., et al. 2017, *Astronomy & Astrophysics*, 602, A107, doi: [10.1051/0004-6361/201629882](https://doi.org/10.1051/0004-6361/201629882)
- Brahm, R., Jordán, A., & Espinoza, N. 2017a, *PASP*, 129, 034002, doi: [10.1088/1538-3873/aa5455](https://doi.org/10.1088/1538-3873/aa5455)
- Brahm, R., Jordán, A., Hartman, J., & Bakos, G. 2017b, *MNRAS*, 467, 971, doi: [10.1093/mnras/stx144](https://doi.org/10.1093/mnras/stx144)
- Brahm, R., Jordán, A., Hartman, J. D., et al. 2015, *AJ*, 150, 33, doi: [10.1088/0004-6256/150/1/33](https://doi.org/10.1088/0004-6256/150/1/33)
- Brahm, R., Espinoza, N., Jordán, A., et al. 2019, *AJ*, 158, 45, doi: [10.3847/1538-3881/ab279a](https://doi.org/10.3847/1538-3881/ab279a)
- Brasseur, C. E., Phillip, C., Fleming, S. W., Mullally, S. E., & White, R. L. 2019, *Astrocute: Tools for creating cutouts of TESS images*. <http://ascl.net/1905.007>
- Bressan, A., Marigo, P., Girardi, L., et al. 2012, *MNRAS*, 427, 127, doi: [10.1111/j.1365-2966.2012.21948.x](https://doi.org/10.1111/j.1365-2966.2012.21948.x)
- Brown, T. M., Baliber, N., Bianco, F. B., et al. 2013, *Publications of the Astronomical Society of the Pacific*, 125, 1031, doi: [10.1086/673168](https://doi.org/10.1086/673168)
- Buchner, J., Georgakakis, A., Nandra, K., et al. 2014, *Astronomy and Astrophysics*, 564, 1, doi: [10.1051/0004-6361/201322971](https://doi.org/10.1051/0004-6361/201322971)
- Burke, C. J. 2008, *The Astrophysical Journal*, 679, 1566, doi: [10.1086/587798](https://doi.org/10.1086/587798)
- Cardelli, J. A., Clayton, G. C., & Mathis, J. S. 1989, *ApJ*, 345, 245, doi: [10.1086/167900](https://doi.org/10.1086/167900)
- Carone, L., Keppens, R., & Decin, L. 2014, *MNRAS*, 445, 930, doi: [10.1093/mnras/stu1793](https://doi.org/10.1093/mnras/stu1793)
- Carone, L., & Pätzold, M. 2007, *Planet. Space Sci.*, 55, 643, doi: [10.1016/j.pss.2006.05.044](https://doi.org/10.1016/j.pss.2006.05.044)
- Carone, L., Mollière, P., Zhou, Y., et al. 2020, *arXiv e-prints*, 1. <https://arxiv.org/abs/2006.05382>
- Castelli, F., & Kurucz, R. L. 2004, *ArXiv e-prints, astro*. <https://arxiv.org/abs/astro-ph/0405087>
- Chen, J., & Kipping, D. 2016, *The Astrophysical Journal*, 834, 17, doi: [10.3847/1538-4357/834/1/17](https://doi.org/10.3847/1538-4357/834/1/17)
- Cheng, W. H., Lee, M. H., & Peale, S. J. 2014, *Icarus*, 233, 242, doi: [10.1016/j.icarus.2014.01.046](https://doi.org/10.1016/j.icarus.2014.01.046)
- Damiani, C., & Lanza, A. F. 2015, *A&A*, 574, A39, doi: [10.1051/0004-6361/201424318](https://doi.org/10.1051/0004-6361/201424318)
- Dawson, R. I., & Johnson, J. A. 2018, *Annual Review of Astronomy and Astrophysics*, 56, 175, doi: [10.1146/annurev-astro-081817-051853](https://doi.org/10.1146/annurev-astro-081817-051853)
- Duncan, D. K., Vaughan, A. H., Wilson, O. C., et al. 1991, *ApJS*, 76, 383, doi: [10.1086/191572](https://doi.org/10.1086/191572)
- Eggleton, P. P., Kiseleva, L. G., & Hut, P. 1998, *The Astrophysical Journal*, 499, 853, doi: [10.1086/305670](https://doi.org/10.1086/305670)
- Espinoza, N., & Jordán, A. 2016, *Monthly Notices of the Royal Astronomical Society*, 457, 3573, doi: [10.1093/mnras/stw224](https://doi.org/10.1093/mnras/stw224)
- Espinoza, N., Kossakowski, D., & Brahm, R. 2019a, *MNRAS*, 490, 2262, doi: [10.1093/mnras/stz2688](https://doi.org/10.1093/mnras/stz2688)
- Espinoza, N., Hartman, J. D., Bakos, G. Á., et al. 2019b, *AJ*, 158, 63, doi: [10.3847/1538-3881/ab26bb](https://doi.org/10.3847/1538-3881/ab26bb)
- Feroz, F., Hobson, M. P., & Bridges, M. 2009, *MNRAS*, 398, 1601, doi: [10.1111/j.1365-2966.2009.14548.x](https://doi.org/10.1111/j.1365-2966.2009.14548.x)
- Ferraz-Mello, S., Rodríguez, A., & Hussmann, H. 2008, *Celestial Mechanics and Dynamical Astronomy*, 101, 171, doi: [10.1007/s10569-008-9133-x](https://doi.org/10.1007/s10569-008-9133-x)
- Foreman-Mackey, D. 2016, *The Journal of Open Source Software*, 24, doi: [10.21105/joss.00024](https://doi.org/10.21105/joss.00024)
- Foreman-Mackey, D., Agol, E., Ambikasaran, S., & Angus, R. 2017, *The Astronomical Journal*, 154, 220, doi: [10.3847/1538-3881/aa9332](https://doi.org/10.3847/1538-3881/aa9332)
- Foreman-Mackey, D., Hogg, D. W., Lang, D., & Goodman, J. 2013, *PASP*, 125, 306, doi: [10.1086/670067](https://doi.org/10.1086/670067)
- Fortney, J. J., Marley, M. S., & Barnes, J. W. 2007, *The Astrophysical Journal*, 659, 1661, doi: [10.1086/512120](https://doi.org/10.1086/512120)
- Freikh, R., Jang, H., Murray-Clay, R. A., & Petrovich, C. 2019, *The Astrophysical Journal*, 884, L47, doi: [10.3847/2041-8213/ab4a7b](https://doi.org/10.3847/2041-8213/ab4a7b)
- Fulton, B. J., Petigura, E. A., Blunt, S., & Sinukoff, E. 2018, *PASP*, 130, 044504, doi: [10.1088/1538-3873/aaaaa8](https://doi.org/10.1088/1538-3873/aaaaa8)
- Gaia Collaboration, Brown, A. G. A., Vallenari, A., et al. 2018, *Astronomy and Astrophysics*, 1, 1
- Gaudi, B. S., & Winn, J. N. 2007, *The Astrophysical Journal*, 655, 550, doi: [10.1086/509910](https://doi.org/10.1086/509910)
- Gill, S., Wheatley, P. J., Cooke, B. F., et al. 2020, *arXiv e-prints*, arXiv:2005.00006. <https://arxiv.org/abs/2005.00006>
- Gladman, B. 1993, *Dynamics of Systems of Two Close Planets*, doi: [10.1006/icar.1993.1169](https://doi.org/10.1006/icar.1993.1169)
- Goldreich, P., & Soter, S. 1966, *Icarus*, 5, 375, doi: [10.1016/0019-1035\(66\)90051-0](https://doi.org/10.1016/0019-1035(66)90051-0)
- Gomes da Silva, J., Santos, N. C., Bonfils, X., et al. 2011, *A&A*, 534, A30, doi: [10.1051/0004-6361/201116971](https://doi.org/10.1051/0004-6361/201116971)
- Hansen, B. M. 2010, *Astrophysical Journal*, 723, 285, doi: [10.1088/0004-637X/723/1/285](https://doi.org/10.1088/0004-637X/723/1/285)
- . 2012, *Astrophysical Journal*, 757, doi: [10.1088/0004-637X/757/1/6](https://doi.org/10.1088/0004-637X/757/1/6)
- Jenkins, J. M., Twicken, J. D., McCauliff, S., et al. 2016, in *Proc. SPIE*, Vol. 9913, *Software and Cyberinfrastructure for Astronomy IV*, 99133E, doi: [10.1117/12.2233418](https://doi.org/10.1117/12.2233418)
- Jones, M. I., Brahm, R., Espinoza, N., et al. 2019, *A&A*, 625, A16, doi: [10.1051/0004-6361/201834640](https://doi.org/10.1051/0004-6361/201834640)
- Jordán, A., Brahm, R., Espinoza, N., et al. 2020, *AJ*, 159, 145, doi: [10.3847/1538-3881/ab6f67](https://doi.org/10.3847/1538-3881/ab6f67)
- Jordán, A., Brahm, R., Bakos, G. Á., et al. 2014, *AJ*, 148, 29, doi: [10.1088/0004-6256/148/2/29](https://doi.org/10.1088/0004-6256/148/2/29)

- Jordán, A., Brahm, R., Espinoza, N., et al. 2020, *The Astronomical Journal*, 159, 145, doi: [10.3847/1538-3881/ab6f67](https://doi.org/10.3847/1538-3881/ab6f67)
- Kaltenegger, L., & Sasselov, D. 2011, *Astrophysical Journal Letters*, 736, 2, doi: [10.1088/2041-8205/736/2/L25](https://doi.org/10.1088/2041-8205/736/2/L25)
- Kaufer, A., Stahl, O., Tubbesing, S., et al. 1999, *The Messenger*, 95, 8
- Kawashima, Y., & Ikoma, M. 2019, *ApJ*, 877, 109, doi: [10.3847/1538-4357/ab1b1d](https://doi.org/10.3847/1538-4357/ab1b1d)
- Kipping, D. M. 2013, *Monthly Notices of the Royal Astronomical Society*, 435, 2152, doi: [10.1093/mnras/stt1435](https://doi.org/10.1093/mnras/stt1435)
- Kozai, Y. 1962, *AJ*, 67, 591, doi: [10.1086/108790](https://doi.org/10.1086/108790)
- Kreidberg, L. 2015, *PASP*, 127, 1161, doi: [10.1086/683602](https://doi.org/10.1086/683602)
- Lainey, V., Arlot, J. E., Karatekin, Ö., & Van Hoolst, T. 2009, *Nature*, 459, 957, doi: [10.1038/nature08108](https://doi.org/10.1038/nature08108)
- Lainey, V., Casajus, L. G., Fuller, J., et al. 2020, *Nature Astronomy*, doi: [10.1038/s41550-020-1120-5](https://doi.org/10.1038/s41550-020-1120-5)
- Lewis, N. K., Knutson, H. A., Showman, A. P., et al. 2013, *Astrophysical Journal*, 766, doi: [10.1088/0004-637X/766/2/95](https://doi.org/10.1088/0004-637X/766/2/95)
- Lidov, M. L. 1962, *Planetary and Space Science*, 9, 719, doi: [https://doi.org/10.1016/0032-0633\(62\)90129-0](https://doi.org/10.1016/0032-0633(62)90129-0)
- Lightkurve Collaboration, Cardoso, J. V. d. M., Hedges, C., et al. 2018, *Lightkurve: Kepler and TESS time series analysis in Python*, *Astrophysics Source Code Library*. <http://ascl.net/1812.013>
- Lubow, S. H. 1991, *ApJ*, 381, 259, doi: [10.1086/170647](https://doi.org/10.1086/170647)
- Luger, R., Agol, E., Foreman-Mackey, D., et al. 2019, *The Astronomical Journal*, 157, 64, doi: [10.3847/1538-3881/aae8e5](https://doi.org/10.3847/1538-3881/aae8e5)
- Lund, M. N., Handberg, R., Davies, G. R., Chaplin, W. J., & Jones, C. D. 2015, *ApJ*, 806, 30, doi: [10.1088/0004-637X/806/1/30](https://doi.org/10.1088/0004-637X/806/1/30)
- McLaughlin, D. B. 1924, *ApJ*, 60, 22, doi: [10.1086/142826](https://doi.org/10.1086/142826)
- Méndez, A., & Rivera-Valentín, E. G. 2017, *The Astrophysical Journal*, 837, L1, doi: [10.3847/2041-8213/aa5f13](https://doi.org/10.3847/2041-8213/aa5f13)
- Méndez, A., & Rivera-Valentín, E. G. 2017, *ApJL*, 837, L1, doi: [10.3847/2041-8213/aa5f13](https://doi.org/10.3847/2041-8213/aa5f13)
- Molaverdikhani, K., Henning, T., & Mollière, P. 2019a, *The Astrophysical Journal*, 883, 194, doi: [10.3847/1538-4357/ab3e30](https://doi.org/10.3847/1538-4357/ab3e30)
- . 2019b, *The Astrophysical Journal*, 873, 32, doi: [10.3847/1538-4357/aafda8](https://doi.org/10.3847/1538-4357/aafda8)
- . 2020, *arXiv e-prints*. <https://arxiv.org/abs/2007.06562>
- Mollière, P., Van Boekel, R., Bouwman, J., et al. 2017, *Astronomy and Astrophysics*, 600, 1, doi: [10.1051/0004-6361/201629800](https://doi.org/10.1051/0004-6361/201629800)
- Mollière, P., van Boekel, R., Dullemond, C., Henning, T., & Mordasini, C. 2015, *The Astrophysical Journal*, 813, 47
- Moses, J. I., Line, M. R., Visscher, C., et al. 2013, *ApJ*, 777, 34, doi: [10.1088/0004-637X/777/1/34](https://doi.org/10.1088/0004-637X/777/1/34)
- Neil, A. R., & Rogers, L. A. 2020, *The Astrophysical Journal*, 891, 12, doi: [10.3847/1538-4357/ab6a92](https://doi.org/10.3847/1538-4357/ab6a92)
- Nelson, B. E., Ford, E. B., Buchner, J., et al. 2020, *The Astronomical Journal*, 159, 73, doi: [10.3847/1538-3881/ab5190](https://doi.org/10.3847/1538-3881/ab5190)
- Noyes, R. W., Hartmann, L. W., Baliunas, S. L., Duncan, D. K., & Vaughan, A. H. 1984, *ApJ*, 279, 763, doi: [10.1086/161945](https://doi.org/10.1086/161945)
- Parmentier, V., Fortney, J. J., Showman, A. P., Morley, C., & Marley, M. S. 2016, *ApJ*, 828, 22, doi: [10.3847/0004-637X/828/1/22](https://doi.org/10.3847/0004-637X/828/1/22)
- Penev, K., Jackson, B., Spada, F., & Thom, N. 2012, *Astrophysical Journal*, 751, doi: [10.1088/0004-637X/751/2/96](https://doi.org/10.1088/0004-637X/751/2/96)
- Petrovich, C., & Tremaine, S. 2016, *The Astrophysical Journal*, 829, 132, doi: [10.3847/0004-637x/829/2/132](https://doi.org/10.3847/0004-637x/829/2/132)
- Petrovich, C., Wu, Y., & Ali-Dib, M. 2019, *The Astronomical Journal*, 157, 5, doi: [10.3847/1538-3881/aaeed9](https://doi.org/10.3847/1538-3881/aaeed9)
- Queloz, D., Henry, G. W., Sivan, J. P., et al. 2001, *Astronomy and Astrophysics*, 379, 279, doi: [10.1051/0004-6361:20011308](https://doi.org/10.1051/0004-6361:20011308)
- Rasio, F. A., & Ford, E. B. 1996, *Science*, 274, 954, doi: [10.1126/science.274.5289.954](https://doi.org/10.1126/science.274.5289.954)
- Ricker, G. R., Winn, J. N., Vanderspek, R., et al. 2014, *Journal of Astronomical Telescopes, Instruments, and Systems*, 1, 014003, doi: [10.1117/1.jatis.1.1.014003](https://doi.org/10.1117/1.jatis.1.1.014003)
- Rodriguez, J. E., Quinn, S. N., Huang, C. X., et al. 2019, *The Astronomical Journal*, 157, 191, doi: [10.3847/1538-3881/ab11d9](https://doi.org/10.3847/1538-3881/ab11d9)
- Rossiter, R. A. 1924, *ApJ*, 60, 15, doi: [10.1086/142825](https://doi.org/10.1086/142825)
- Schlecker, M. 2016, *Master's Thesis*, doi: [10.5281/zenodo.221659](https://doi.org/10.5281/zenodo.221659)
- Schlecker, M., Mordasini, C., Emsenhuber, A., et al. 2020, *Astronomy & Astrophysics*, 1, <https://arxiv.org/abs/2007.05563>
- Seager, S., Richardson, L. J., Hansen, B. M. S., et al. 2005, *ApJ*, 632, 1122, doi: [10.1086/444411](https://doi.org/10.1086/444411)
- Southworth, J. 2011, *Monthly Notices of the Royal Astronomical Society*, 417, 2166, doi: [10.1111/j.1365-2966.2011.19399.x](https://doi.org/10.1111/j.1365-2966.2011.19399.x)
- Stevenson, K. B. 2016, *ApJL*, 817, L16, doi: [10.3847/2041-8205/817/2/L16](https://doi.org/10.3847/2041-8205/817/2/L16)
- Sullivan, P. W., Winn, J. N., Berta-Thompson, Z. K., et al. 2015, *Astrophysical Journal*, 809, 77, doi: [10.1088/0004-637X/809/1/77](https://doi.org/10.1088/0004-637X/809/1/77)

- Triaud, A. H. M. J. 2018, *Handbook of Exoplanets*, 1375, doi: [10.1007/978-3-319-55333-7_2](https://doi.org/10.1007/978-3-319-55333-7_2)
- Tsai, S.-M., Kitzmann, D., Lyons, J. R., et al. 2018, *ApJ*, 862, 31, doi: [10.3847/1538-4357/aac834](https://doi.org/10.3847/1538-4357/aac834)
- Vallat, R. 2018, *The Journal of Open Source Software*, 3, 1026
- Venot, O., Hébrard, E., Agúndez, M., et al. 2012, *A&A*, 546, A43, doi: [10.1051/0004-6361/201219310](https://doi.org/10.1051/0004-6361/201219310)
- Venot, O., Parmentier, V., Bleic, J., et al. 2020, *ApJ*, 890, 176, doi: [10.3847/1538-4357/ab6a94](https://doi.org/10.3847/1538-4357/ab6a94)
- Yoder, C. F., & Peale, S. J. 1981, *Icarus*, 47, 1, doi: [10.1016/0019-1035\(81\)90088-9](https://doi.org/10.1016/0019-1035(81)90088-9)
- Zechmeister, M., & Kürster, M. 2009, *Astronomy and Astrophysics*, 496, 577, doi: [10.1051/0004-6361:200811296](https://doi.org/10.1051/0004-6361:200811296)